Supplementary Information

Large-scale lithography-free metasurface with spectrally tunable super absorption

Kai Liu[1], Xie Zeng[1], Suhua Jiang[2], Dengxin Ji[1], Haomin Song[1], Nan Zhang[1], Qiaoqiang Gan[1]*

1. Department of Electrical Engineering, The State University of New York at Buffalo, Buffalo, NY 14260.
2. Department of Materials Science, Fudan University, Shanghai 200433, China
*email: qqgan@buffalo.edu.

1. Diameter distribution of directly-sputtered Ag NPs

According to SEM images shown in Fig. 1, randomly distributed Ag NPs were obtained from the direct sputtering process. The statistic distribution of the NPs can be controlled by changing the deposited mass thickness, as shown in Fig. S1. According to previous reports [S1-S3], the resonant peak wavelength of MDM super absorbers strongly depends on the lateral dimension (i.e. diameter/length) of the periodic or random distributed nanopatterns. Here, the spectral position of the resonant peak is mainly determined by the dominant diameter of Ag NPs. One can see from Fig. S1 that the dominant diameter ranges from 10-15 nm to 30-35 nm as the deposited mass thickness increases from 0.8 to 4.0 nm, and therefore resulting in the red-shift of the absorption peaks for samples MA1-MA5 (see Fig. 2a). Moreover, due to the relatively wide distribution of the particle diameter, broader band optical absorption resonances were obtained in these directly-sputtered samples compared with their periodically patterned counterparts [S4- S6].

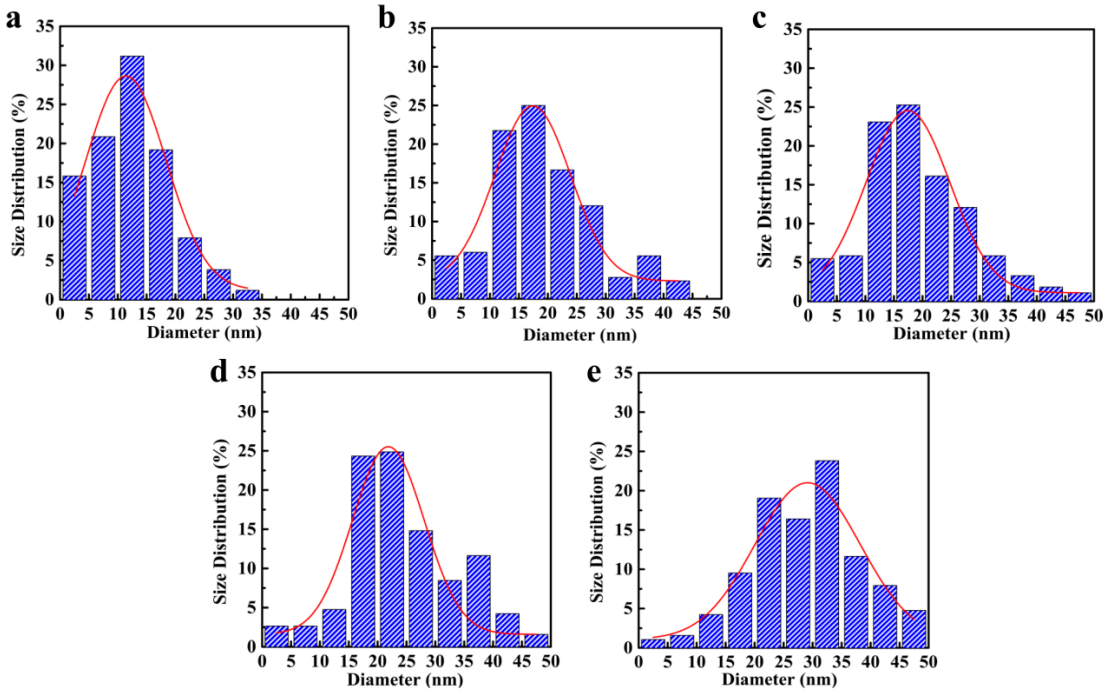

Figure S1. Size distributions of direct-deposited Ag NPs with different nominal mass thicknesses of (**a**) 0.8 nm, (**b**) 1.6 nm, (**c**) 2.4 nm, (**d**) 3.2 nm, and (**e**) 4.0 nm, respectively. The size distribution percentage is calculated by the ratio of particle counts in a specific diameter range to the total number of Ag NPs from the SEM images shown in Fig. 1. The red lines are Gaussian fittings of the size distribution of NPs.

2. Scattering effect of the directly-deposited metasurfaces

The reflection spectra of metasurfaces were characterized by a microscopic FTIR with a 15X objective lens (NA=0.4), which can only collect the reflected/scattered light within the spatial angle of 23.6˚. To demonstrate the accuracy of the measured reflection and absorption spectrum, we employed another three objective lenses (NA=0.3, 0.6 and 0.95, corresponding to the collection angles of 17.4˚, 36.9˚ and 71.8º, respectively) in an optical microscope (OLYMPUS IX81) coupled with a compact spectrometer (Ocean Optics, Jaz) to measure the reflection spectrum of sample MA4, as shown in Fig. S2a. One can see that the measured reflection spectra under the collection angles of 36.9˚ and 71.8˚ are approximately identical, indicating that all the scattered signals can be safely collected within the angle of 36.9˚. Although the reflection spectrum observed by the microscopic FTIR system is slightly different from the one observed within the collection angle of 36.9˚, the spectral position and the absolute intensity at the resonance position is almost identical, indicating the absorption spectra observed in the microscopic FTIR system is accurate to demonstrate the resonant super absorption.

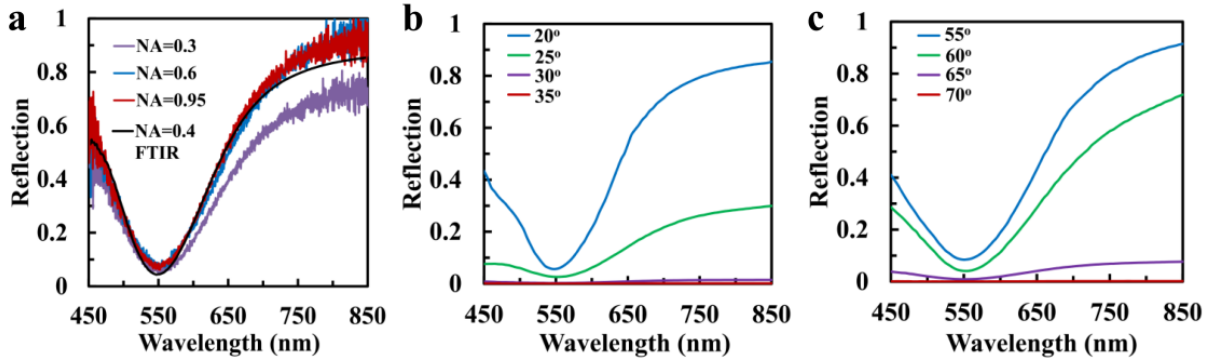

Figure S2. (**a**) Reflection spectra of sample MA4 measured by four objective lenses with NA=0.3, 0.4, 0.6 and 0.95, respectively. (**b**) and (**c**) are measured angle-dependent reflection/scattering spectra of sample MA4 with a fixed incident angle at (**b**) 15˚ and (**c**) 50˚, respectively.

To reveal the direction of the scattered light, we employed an angular-tunable stage (Bruker, A513/Q) to measure the angle-dependent reflection/scattering spectra of sample MA4 with a fixed incident angle. As shown in Fig. S2b, the incident angle is fixed at 15º and the collection angle is tuned to 20˚, 25˚, 30˚,

and 35˚, respectively. One can see that little reflection signal can be measured beyond the angle of 30˚. For a large incident angle of 50˚, when the collection angle is tuned to 55˚, 60˚, 65˚, and 70˚, more scattering signal can be observed at longer wavelengths, explaining the slight difference in this spectral region observed in Fig. S2a. Due to the omnidirectional absorption feature of the meta-absorber (see Fig. S3d), there is little scattering signal observed at the resonant wavelength. Consequently, the absorption spectra observed by the microscopic FTIR system can represent the optical properties of the proposed metasurface accurately at the resonant wavelength.

3. Modeling of optical properties of metasurface structures

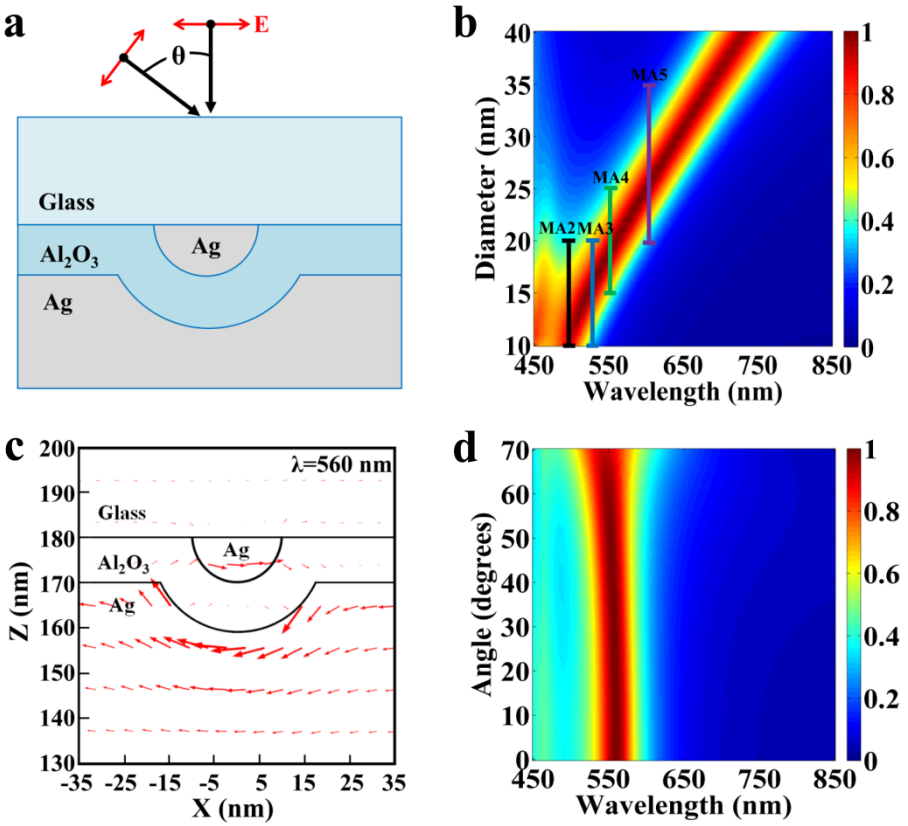

Figure S3. (**a**) Conceptual illustration of the three-layered metamaterial absorber structure. (**b**) Absorption spectra as the function of NP diameters, D, from 10 nm to 40 nm. Four bars indicate the NP diameter ranges of samples MA2-MA5 obtained from Fig. S1. (**c**) Modeled displacement current density of sample NM3 (i.e. D=20 nm). (**d**) Simulated absorption spectra of NM3 as the function of the incident angle.

Fig. S3a illustrates the inverted 2D meta-absorber structure modeled using COMSOL Multiphysics®. The structure consists of a top glass layer, a semicircular Ag nanoparticle, a 10-nm-thick Al_2O_3 film and

an optically thick Ag ground plate. A TM-polarized plane wave is employed to illuminate the structure from the glass side at normal or oblique incident directions. The absorption spectra are plotted in Fig. S3b as the function of the NP diameter, showing that the resonant wavelength is tuned from 494 nm to 732 nm as the particle diameter increases from 10 nm to 40 nm. The observed resonant peak positions of samples MA2-MA5 were marked with vertical bars to indicate dominant diameter ranges for each sample (see Fig. S3b), showing reasonably good agreement with the theoretical modeling. The resonant position of sample MA1 was not plotted since it is beyond the spectral region available for our measurement system. To demonstrate the nature of the absorption resonance explicitly, the displacement current density of model NM3 (i.e. D=20 nm) is plotted in Fig. S3c. A circulation of current is excited between the Ag nanopattern and the ground plate, forming the magnetic resonance [S2, S7- S9]. To further reveal the angular dependence of the optical response of NM3, we modeled its absorption resonance as the function of the incident angle as shown in Fig. S3d. Due to the angle-independent coupling between the incident magnetic field and the excited magnetic resonance mode[S7], the super absorption peak over 85% can be retained up to 70˚. Therefore, the spectrally tunable perfect absorption resonance supported by the metasurface structure is also omnidirectional, as revealed by experimental characterizations shown in Figs. 2e and 4b.

4. Post thermal treatment

To overcome the percolation threshold limitation of the directly deposited Ag films, post thermal annealing processes can be introduced to transform the mesh network back to isolated Ag NPs and further broaden the tunability of NP dimensions. Here we first deposited Ag layers with mass thicknesses of 9.6, 11.2, 12.8 and 14.4 nm on top of microscope glass substrates, as shown in the left panels of Figs. S4a-S4d (denoted as M6-M9). One can see that connected metal networks were obtained. When these metal mesh networks were covered by 20-nm-thick Al_2O_3 spacer films and optically thick Ag ground plates to form the three-layered MDM structures (denoted as RA6-RA9 in Fig. S4), their optical absorption properties are relatively weak as shown by the dashed lines in Fig. S4e, indicating that the magnetic resonances were not excited efficiently or the critical coupling condition was not met. We then employed the post thermal annealing to further manipulate the morphologies of these connected metal meshes. As shown in Fig. S4, samples M6-M9 were annealed in a N_2 ambient at the temperature of 300˚C for 30 minutes. As a result, the connected mesh networks were transformed into isolated NPs (see SEM images of samples MA6-MA9). The optical absorption spectra of the three-layered MDM structure based on these annealed NPs were characterized as shown by solid lines in Fig. S4e. One can see that obvious absorption resonances were obtained with the absorption peaks of 60.9%, 62.4%, 66.9%, and 63.9% in the near infrared spectral

region from 921 nm to 1339 nm, respectively. The relatively low absorption is potentially related to the non-uniform shape of the metal particles. Further exploration and optimization of IR super absorbers are still under investigation using oblique angle depositions [S10, S11].

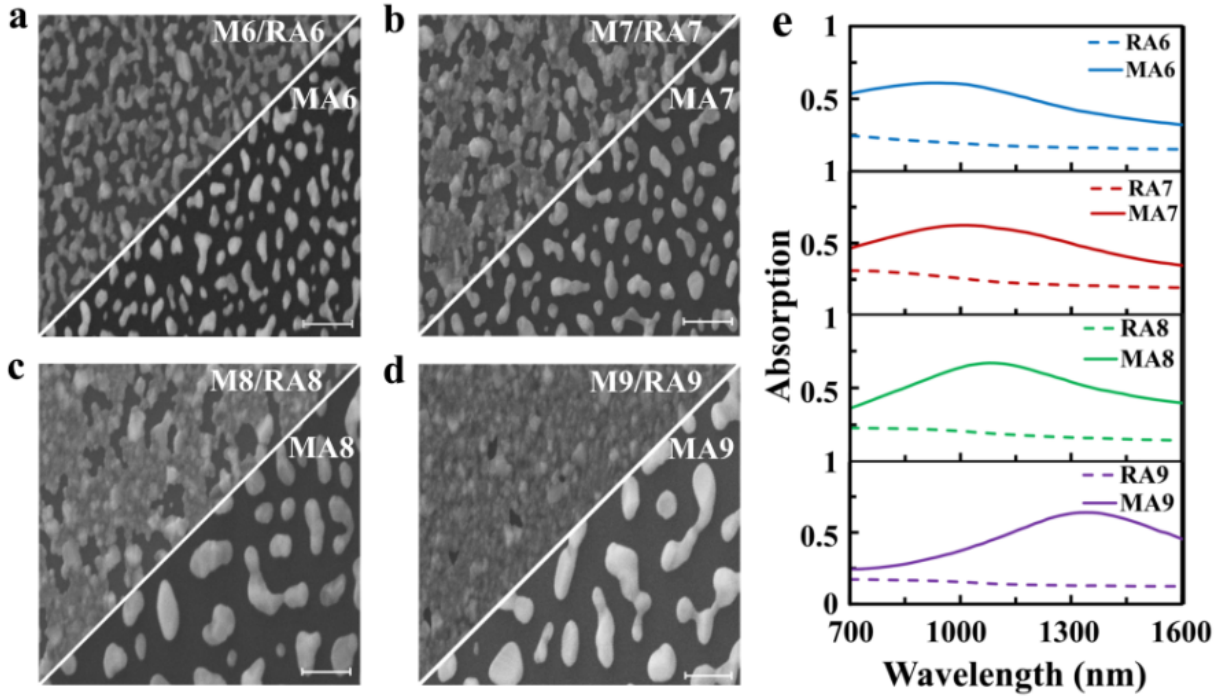

Figure S4. (**a**)-(**d**) Left corners show SEM images of the directly-deposited metal films (i.e. samples M6-M9) with nominal mass thicknesses of (**a**) 9.6 nm, (**b**) 11.2 nm, (**c**) 12.8 nm and (**d**) 14.4 nm, respectively. Right corners show the surface morphologies of NPs after the thermal treatment. The scale bar is 400 nm. (**e**) Absorption spectra of three-layered MDM structures based on the connected metal mesh networks (see dotted lines, i.e. samples RA6-RA9) and thermal annealed NPs (see solid lines, i.e. samples MA6-MA9).

5. Fabrication of graded metasurface absorbers

The sputtering system configuration for the directional deposition of graded metasurfaces is illustrated in Fig. S5a. The distance between the Ag target center and the substrate stage is H=8.2 cm, while the central axis of the sputtering beam is aligned with the substrate surface at an angle of θ=70˚. The local mass thickness increases gradually from the left edge to the right edge and form the graded variable NP layers (i.e. samples GR1 and GR2 in Fig. 3a). In our experiment, the nominal mass thickness of the deposited metal film is 2.4 nm and 3.2 nm for samples GR1 and GR2, respectively. Figs. S5b and S5c are measured absorption spectra for samples GR1 and GR2, respectively, showing the best optical absorption of ~37% (indicated by the empty circles), which is relatively weak.

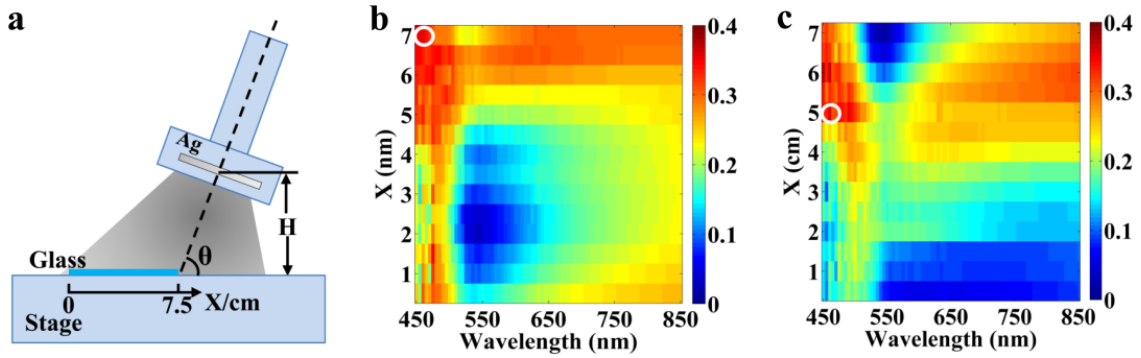

Figure S5. (**a**) Configuration schematic of the sputtering chamber for the graded NP deposition. In our system, H=8.4 cm and θ=70˚. (**b**) and (**c**) show the measured spatial-dependent absorption spectra of reference graded samples (**b**) GR1 and (**c**) GR2, respectively. Empty circles indicate the highest absorption peaks of GR1 and GR2.

6. Optical characterization of glass and flexible PEN substrates

As shown in Fig. 4, the optical absorption of flexible metasurface absorbers are slightly lower than those fabricated on glass substrates shown in Figs. 2 and 3 due to the higher reflection of the PEN material. As shown in Fig. S6, we measured the optical reflection and transmission spectra of a glass slide and a PEN substrate. One can see that the reflection from the flexible substrate (red dashed line) is 10-16% in the visible to near-IR spectral region, which is 6-11% higher than that for a glass substrate (blue dashed line). This higher reflection at the air-PEN interface results in the reduced peak absorption, and therefore degrading the visual contrast of the uniform and graded flexible meta-absorbers.

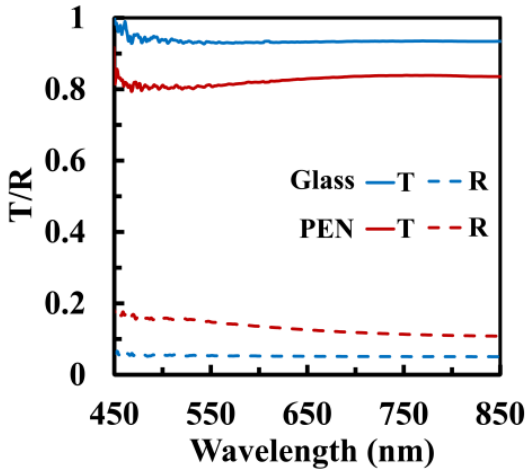

Figure S6. Transmission (solid curves) and reflection (dashed curves) properties of a glass slide (blue lines) and a flexible PEN substrate (red lines).

References

[S1] Kumar, K., Duan, H., Hegde, R. S., Koh, S. C., Wei, J. N. & Yang, J. K. Printing colour at the optical diffraction limit. *Nat. Nanotechnol.* **7**, 557-561 (2012).

[S2] Tittl, A., Mai, P., Taubert, R., Dregely, D., Liu, N. & Giessen, H. Palladium-based plasmonic perfect absorber in the visible wavelength range and its application to hydrogen sensing. *Nano Lett.* **11**, 4366-4369 (2011).

[S3] Cheng, C., Abbas, M. N., Chiu, C., Lai, K. Shih, M. & Chang, Y. Wide-angle polarization independent infrared broadband absorbers based on metallic multi-sized disk arrays. *Opt. Express* **20**, 10376-10381 (2012).

[S4] Wu, C. & Shvets, G. Design of metamaterial surfaces with broadband absorbance. *Opt. Lett.* **37**, 308-310 (2012).

[S5] Bouchon, P., Koechlin, C., Pardo, F., Haidar, R. & Pelouard, J. Wideband omnidirectional infrared absorber with a patchwork of plasmonic nanoantennas. *Opt. Lett.* **37**, 1038-1040 (2012).

[S6] Cui, Y., Xu, J., Fung, K. H., Jin, Y., Kumar, A., He, S. & Fang, N. X. A thin film broadband absorber based on multi-sized nanoantennas. *Appl. Phys. Lett.* **99**, 253101 (2011).

[S7] Liu, N., Mesch, M., Weiss, T., Hentschel, M. & Giessen, H. Infrared perfect absorber and its application as plasmonic sensor. *Nano Lett.* **10**, 2342-2348 (2010).

[S8] Wu, C., Neuner, B. & Shvets, G. Large-area wide-angle spectrally selective plasmonic absorber. *Phys. Rev. B* **84**, 075102 (2011).

[S9] Hao, J., Zhou, L. & Qiu, M. Nearly total absorption of light and heat generation by plasmonic metamaterials. *Phys. Rev. B* **83**, 165107 (2011).

[S10] Fu, J., Collins, A. & Zhao, Y. Optical properties and biosensor application of ultrathin silver films prepared by obique angle deposition. *J. Phys. Chem. C* **112**, 16784-16791 (2008).

[S11] He, Y., Fu, J. & Zhao, Y. Oblique angle deposition and its application in plasmonics. Front. Phys. DOI 10.1007/s11467-013-0357-1.